Effects of NO_2 aging on bismuth nanoparticles and bismuth-loaded silica xerogels for iodine capture

Karthikeyan Baskaran[a1], Casey Elliott[a1], Muhammad Ali[a], Jeremy Moon[a], Jade Beland[a], Dave Cohrs[a], Saehwa Chong[b], Brian J. Riley[b], Dev Chidambaram[a,c], Krista Carlson[a,*]

[a]Department of Chemical and Materials Engineering, University of Nevada, Reno, Reno, Nevada 89557, USA

[b]Pacific Northwest National Laboratory (PNNL), Richland, Washington 99532, USA

[c]Nevada Institute for Sustainability, University of Nevada, Reno, Reno, Nevada, 89557-0388, USA

[1]Both authors contributed equally to this work.
*Corresponding author

Abstract:

The capture of long-lived radioactive iodine (^{129}I) from oxidizing off-gasses produced from reprocessing used nuclear fuel is paramount to human health and environmental safety. Bismuth has been investigated as a viable iodine getter but the phase stability of bismuth-based sorbents in an oxidizing environment have not yet been researched. In the current work, bismuth nanoparticle-based sorbents, as free particles (Bi-NPs) and embedded within silica xerogel monoliths made with a porogen (TEO-5), were exposed to $I_{2(g)}$ before and after aging in 1 v/v% NO_2 at 150 °C. For unaged sorbents, BiI_3 was the dominant phase after iodine capture with 8-30 mass% BiOI present due to native Bi_2O_3 on the surface of the unaged nanoparticles. After 3 h of aging, 82 mass% of the Bi-NPs was converted to Bi_2O_3 with only a small amount of iodine captured as BiOI (18 mass%). After aging TEO-5 for 3 h, iodine was captured as both BiI_3 (26%) and BiOI (74%) and no Bi_2O_3 was detected.”. Additionally, bismuth lining the micrometer-scale pores in the TEO-5 led to enhanced iodine capture. In a subsequent exposure of the sorbents to NO_2 (secondary aging), all BiI_3 converted to BiOI. Thus, direct capture of iodine as BiOI is desired (over BiI_3) to minimize loss of iodine after capture.

Keywords:

- Bismuth sorbents
- NO_2 aging
- Iodine capture
- Silica xerogel
- Bismuth oxyhalide

1. Introduction

Continuous growth in demands for energy has fueled the exploration, development, and implementation of low-carbon energy sources [1]. As such, nuclear power contributes to over 20% of the

U.S. electricity demand and is among the top alternative energy sources to burning fossil fuels [2]. Nuclear power is positioned to play a crucial role for the national grid decarbonization plans in the United States [3]. To ensure continued utilization of current nuclear plants and next generation designs, the reprocessing of used nuclear fuel (UNF) is being considered.

One reprocessing option is using the PUREX (plutonium uranium extraction) process, an aqueous method to recover uranium and plutonium from UNF [4]. During the PUREX process, radioactive volatiles, such as ^{3}H, ^{14}C, ^{85}K, and ^{129}I, are released into off-gas streams. As these radionuclides can have adverse effects on the environment, their capture and management are paramount to the success of these nuclear processes [5, 6]. Capturing ^{129}I before releasing the off-gas is of primary importance with respect to U.S. regulations because of its mobility in the environment and long half-life of 15.7 million years [7]. Both inorganic and organic iodine-bearing species can be released at multiple points during reprocessing [8]. The complexity of the off-gas streams, which can include variations in the form and concentration of iodine, makes it challenging to find sorbents suitable for controlled and sustained capture. An example of one such stream is the off-gas that is produced during an advanced tritium pretreatment (ATPT) process, employed to reduce the release of tritium [9]. During this processes, the sheared fuel is exposed to ~75 vol% NO_2 gas at elevated temperatures to release tritium contained within the fuel matrix [10]. A low concentration of iodine is also released during this process [8]. A potential iodine sorbent for this off-gas stream would have to capture dilute concentrations in highly oxidizing conditions.

Extensive efforts have been made to develop the ideal sorbent for operation in oxidizing off-gas streams, which requires chemisorption to immobilize and/or retain the radioiodine as the loaded sorbent is converted into a waste form [11-15]. To that end, the optimal iodine capture performance (i.e., loading capacity of chemisorbed iodine under static and saturated conditions) of silver-exchanged mordenite [16-21], and silver-functionalized xerogels [7] and aerogels [7, 22-25], have been extensively studied. These silver-based sorbents have also been studied to understand and evaluate the change in iodine capture performances in the sorbents "aged" with NO_x exposure. Decline in performance of silver-based sorbents were seen as silver interacts with NO_x to form nitrosyl surface compounds. These nitrosyl compounds compete for the iodine adsorption sites and reduce the capture capacity [20].

Alternatives to silver are being explored due to the reduction of performance of Ag-based sorbents in the presence of NO_2 and because silver is an expensive metal whose disposition is controlled by the United States Environmental Protection Agency [26, 27]. Bismuth-based sorbents, such as SBA-15 [28, 29], mordenite [30], functionalized carbon foam [31], functionalized metallic foam [32], carbon nanofiber [33, 34], and graphene [35] have been explored because bismuth is far less expensive and does not have disposal restrictions. Bismuth-based sorbents have shown great promise with reports of iodine trapping capacities greater than commercial Ag-exchanged zeolites under the same experimental conditions (468 mg g^{-1} versus 305 mg g^{-1} for Ag-faujasite) [26]. The primary compound formed when Bi reacts with $I_{2(g)}$ is BiI_3. Bismuth embedded in mesoporous silica functionalized with thiol (-SH) groups was reported to have an even higher iodine loading capacity at up to 540 mg g^{-1} [29]. In this case, Bi_2S_3 participated in the chemisorption of iodine to produce thermodynamically stable compounds even in the presence of $O_2(g)$, and the formation of BiI_3 was more favorable than Bi_2O_3.

Thermodynamic modeling software (HSC chemistry) in Table 1 shows spontaneous formation of Bi_2O_3 and BiI_3, indicating the possibility for oxidation before or during iodine capture. However, bismuth was also thought to have potential for steady performance in the oxidizing atmospheres due to its ability to form bismuth oxyhalide compounds [17]. Together, Bi and Bi_2O_3 can capture $I_{2(g)}$ by forming BiOI and Bi_5O_7I [29]. BiOI captured using Bi and Bi_2O_3 was found to be stable up to 350 °C, after which transformation to Bi_5O_7I is likely. As BiI_3 is highly susceptible to oxidation and moisture, understanding the performance of bismuth compounds in an oxidizing environment before and after iodine capture is necessary to improve the lifetime of these sorbents and for long-term iodine storage with both chemical and mechanical stability.

Table 1. Reactions calculated using HSC

HSC Reaction Equations			
Primary Aging Oxidation Reactions	***ΔG(kJ,150°C)***	***Spontaneous***	***Eq #***
$8Bi + 6NO_2(g) = 4Bi_2O_3 + 3N_2(g)$	-2163.19	*Y*	*5*
$2Bi + 3NO_2(g) = Bi_2O_3 + 3NO(g)$	-373.987	*Y*	*6*
Iodine Loading Reactions			
$Bi + 1.5\ I_2(g) = BiI_3$	-150.356	*Y*	*7*
$Bi_2O_3 + Bi + 1.5\ I_2 = 3BiOI$	-225.518	*Y*	*8*
$BiI_3 + Bi_2O_3 = 3BiOI$	-79.9939	*Y*	*9*
$0.5\ Bi_2O_3 + 0.5\ I_2(g) = BiOI + 0.25\ O_2(g)$	-1.37654	*Y/N*	*10*
$2Bi + O_2(g) + I_2(g) = 2BiOI$	-455.19	*Y*	*11*
$Bi_2O_3 + 3I_2(g) = 2BiI_3 + 1.5O_2(g)$	151.7244	*N*	*12*
Secondary Aging Reactions			
$BiI_3 + 0.5\ NO_2(g) = BiOI + I_2(g) + 0.25\ N_2(g)$	-106.692	*Y*	*13*
$BiI_3 + NO_2(g) = BiOI + I_2(g) + NO(g)$	-51.0908	*Y*	*14*
$8BiOI + 2NO_2(g) = 4Bi_2O_3 + 4I_2(g) + N_2(g)$	-106.805	*Y*	*15*
$2BiOI + NO_2(g) = Bi_2O_3 + I_2(g) + NO(g)$	28.90307	*N*	*16*
$2Bi_2O_3 + 2NO_2(g) = 2Bi_2O_5 + N_2(g)$	-256.885	*Y*	*17*
$Bi_2O_3 + 2NO_2(g) = Bi_2O_5 + 2NO(g)$	-17.2381	*Y*	*18*
Comparable Reactions at 150°C			
$Ag + 0.5I_2(g) = AgI$	*-69.0486*	*Y*	*19*

Another challenge that has yet to be addressed with low-density, high specific surface area (SSA) sorbents is how to form these materials into viable media that can be incorporated into an industrial facility. For example, aerogels are often studied at the bench-scale using batch experiments or packed-bed systems [36-40]. However, aerogels are low density, have low mechanical strength, tend to agglomerate, and are likely to lead to non-uniform flow (i.e., channeling) at a larger scale and higher flow rates [41-43]. This behavior would lead to unpredictable and lower-than-desired decontamination factors, as well as potential difficulties with maintenance and materials handling [44, 45]. These issues could be eliminated by using highly permeable membranes that minimize the pressure drop and sustain flow without channeling while maintaining higher mechanical strength and integrity [44, 46]. Xerogels engineered to have micrometer-sized pores are a type of high specific surface area material that could be used as membranes [47]. Xerogels are produced by ambient pressure drying instead of critical point (supercritical) drying as used in aerogel synthesis. Structural changes that occur during drying typically result in xerogels that have enhanced strength but with fewer processing steps.

The goal of this study was to evaluate the $I_{2(g)}$ capture performance of bismuth nanoparticles, as free particles (Bi-NPs) and embedded within silica xerogel monoliths, before and after aging in flowing 1 v/v% NO_2 (balance N_2) at 150 °C. This composition of NO_2 was chosen to be the first step towards understanding the behavior of bismuth metal sorbents in a prototypical off-gas environment. Based on our previous work, mechanically stable xerogel membranes were made with cost effective and environmentally friendly soybean oil as porogen. The addition of soybean oil created hierarchical pore structure in the xerogel membranes [47]. A secondary aging treatment was performed to understand the stability of the bismuth-iodine phases. This information is important to understand the long-term stability of the sorbent during storage or if the reprocessing plant is idling. Sorbents were characterized with field emission gun scanning electron microscopy (SEM), energy dispersive X-ray spectroscopy (EDS), X-ray diffraction (XRD), thermogravimetric analysis (TGA), differential scanning calorimetry (DSC), Fourier transform infrared (FTIR) spectroscopy, and X-ray photoelectron spectroscopy (XPS).

2. Experimental

2.1. Materials

TEOS (97%; CAS # 78–10–4) was acquired from TCI America. Heptane (99%; C_7H_{16}; CAS # 142–82–5), deionized water (CAS # 7732–18–5), and absolute ethanol (C_2H_6O; CAS # 64–17–5; 200 proof) were acquired from Fisher Scientific. Ammonium fluoride (98%; NH_4F; CAS # 12125–01–8), and ammonium hydroxide (reagent grade; NH_4OH; CAS # 1336–21–6) were acquired from Sigma Aldrich. Bismuth nanoparticles (99.9%; < 100 nm) and bismuth oxide nanoparticles (99.9%; <200 nm) were acquired from SkySpring Nanomaterials, Inc. Soybean oil was purchased from the local grocery store as white label vegetable oil. Sylgard 184 silicone elastomer was obtained from DOW Chemical Company. Helium gas and 1% nitrogen dioxide (NO_2) balance nitrogen (N_2) were obtained from Airgas. A granular Ag-faujasite zeolite (AgX) (IONEX Ag400) was obtained from Molecular Products, Inc.

2.2. Preparation of xerogels

TEOS-based silica xerogels were prepared using the sol-gel method published in our previous work [47] and compositions used for this work are described in table 2. In summary, to make a silica alcogel, 1.2 M TEOS was used as silica precursor and 7.2 M water (with 10.9 mM NH_4F and 0.131 M NH_4OH as a catalyst) was used as hydrolysis solution. Both the precursor and hydrolysis solutions was prepared in separate containers with 200 proof absolute ethanol as the solvent. Then, 100 µL of soybean oil per mL of sol-gel solution was added to the precursor solution as a porogen [47]. Six sets of xerogels were created with 0 w/v %, 2 w/v % and 5 w/v % Bi to sol-gel solution with and without porogen. Xerogels made without the porogen (soybean oil) were named as TE, TE-2 and TE-5 for 0 w/v %, 2w/v % and 5 w/v % Bi loading, respectively, and TEO, TEO-2 and TEO-5 for 0 w/v %, 2w/v % and 5 w/v % Bi loading with the oil porogen, respectively. The precursor and hydrolysis solutions were mixed, vortexed for 30 s, and poured into a mold, made by cutting the top of a 10 mL flat plunger plastic syringe with 10-mm inner diameter. After 10 min, the gels were removed from the mold and transferred to a solution of heptane for 24 h to remove the oil. The gels were then dried at ambient pressure for another 24 h, and then heat-treated at 150°C for 24 h to remove residual oil and solvent.

Table 2. sorbent sample list

Sample ID	Substrate	Porogen added	Bi-NPs added
TE	silica xerogel		
TEO	silica xerogel	100 µl oil	
TE-2	silica xerogel		0.02 g per mL of precursor
TEO-2	silica xerogel	100 µl oil	0.02 g per mL of precursor
TE-5	silica xerogel		0.05 g per mL of precursor
TEO-5	silica xerogel	100 µl oil	0.05 g per mL of precursor
Bi-NPs	free bismuth nanoparticles		0.05 g

2.3. Characterization

The surface morphologies of silica xerogels were studied using an SEM (JSM-7001F, JEOL USA, Inc. Peabody, MA) with EDS using a Bruker xFlash 6|60 detector (Bruker AXS Inc., Madison, WI). XRD patterns were obtained using a Rigaku Smartlab 3 kW X-ray diffractometer with copper Kα radiation. TGA and DSC analysis were performed with a Netzsch STA 449F3 using ultra-high-purity (UHP) air and protective argon and ramped at 10°C/min. Organic materials were identified using two different FTIR and attenuated total reflectance (ATR) instruments (ThermoScientific Nicolet iN10 and 380). X-ray photoelectron spectroscopy (XPS) spectra were collected using a ThermoFisher Scientific Nexsa G2 Surface Analysis System with a monochromatic Al X-ray source. Spectra were charge corrected to the C 1s peak of adventitious carbon at 284.8 eV. Depth profiling was conducted using a 1000 eV argon ion source for 20-100 seconds. Thermo Avantage software was used for data analysis and reporting. Gravimetric analysis was performed using a VWR-164AC analytical scale with 0.1 mg readability and repeatability. Permeabilities of samples were found using a custom design described in Section 2.4. The SSA values were measured with a Micromeritic 3Flex with nitrogen gas.

2.4. Helium permeability measurements

Helium permeabilities of xerogel samples were measured through steady state gas flow measurements using a custom designed flow setup (Fig. S1 in SI). Polymethylsiloxane holders were cured in 3D-printed molds designed specifically to house an as-prepared xerogel with a good fit. Xerogels were sealed into the cured holder using a silicone adhesive, dried for 24 hours, and vacuum desiccated to remove moisture before testing. Xerogel holders were inserted into an airtight glass tube and connected in line with the helium gas-flow system. A working flow range of helium (0.01–1.00 standard cubic centimeter per second by volume [sccsv]) was controlled using an Omega FMA-2618A flow controller (0.8% accuracy) and an Omega FMA-2617A flow meter (0.8% accuracy) was used to observe the resulting pressure drop. Once a linear regime was established, Darcy's law of fluid flow (Eq.1) through a porous medium was applied at 0.02 ± 0.00016 sccsv, a flow rate within the linear working range to calculate permeability:

$$K = \frac{Q * \eta * L}{\Delta P * A} \quad (1)$$

where the length of the porous medium is L (cm), the pressure drop is ΔP (g cm^{-2} s), the volumetric flow rate is Q (cm s^{-1}), the fluid viscosity is η (g cm^{-1}s^{-1}), and the permeability is K (cm^2) converted into m^2 for final reporting. Xerogels were checked for cracks before and after testing through backlit and standard optical photography, and cracked samples were not included in the reported results.

2.5. Iodine capture performance

The optimal iodine capture performances of the xerogels and Bi-NP sorbents were quantified by determining the quantity of chemisorbed iodine under saturated conditions. Before loading, samples were kept under vacuum to prevent moisture accumulation. Samples were loaded into glass vials with known tare masses, and the sample masses were recorded as (m_s). Triplicates of samples in glass vials, an empty glass vial, and a glass vial with 1 g solid iodine were placed in a 1 L PFA (perfluoroalkoxy) jar with a lid (Savillex). The Savillex jar was placed in the oven preheated to 150 ± 2°C, and the reaction was carried out for 24 hours. The mass of iodine was chosen to be in excess of the total sample mass to provide a saturated environment, resulting in an iodine cloud when the container was opened immediately after removal from the oven. After the reaction, the sample vials were placed uncovered back in the oven to remove physisorbed iodine for 1 h. The resulting mass change in samples were recorded as iodine mass gained in mg (m_i). The mass percentage of iodine in the final sample can be calculated using Eq. 2, and the iodine sorption capacity (Q_e in mg g^{-1}) of samples can be calculated using Eq. 3. For samples that underwent mass change during NO_2 exposure, m_s is given as the mass of the sorbent or mass of bismuth after oxidizing. Even though these samples show BiOI as a reaction product, Eq. 8 and 9 (Table 1 in Section 1) stoichiometry show the mass change is due only to the capture of iodine.

$$Mass\ of\ I_2\ captured\ \% = \frac{m_i}{m_i + m_s}\ x\ 100 \quad (2)$$

$$Q_e = \frac{m_i}{m_s} \quad (3)$$

2.6. NO_2 aging

Before aging, samples were kept under vacuum to prevent moisture accumulation. A dynamic system (Fig. S2 in SI) was used to age Bi-NPs and TEO-5 in 1 v/v% NO_2 (balance N_2) at 150 °C before and after iodine loading. Samples were loaded into glass vials with known tare masses, and the masses of the sample (m_s). Triplicates of each sample were loaded into the 1-L Savillex jar. The jar was placed in an oven preheated to 150 ± 2°C and connected to the gas supply. Then, NO_2 was introduced at 20 sccsv for 1 min using an Alicat MQS-100SLPM mass flow controller (2% accuracy) to saturate the container, then reset to 1 sccsv for the duration of the aging test. Once the aging time was reached, the gas supply was switched to UHP air, and the container was purged for 2 min at 20 sccsv. Finally, the gas supply was closed, and the samples were removed for characterization. The final mass of the samples was recorded as mass (m_f). The percentage of weight gain due to oxygen in the final sample was calculated using Eq. 4:

$$Sorbent\ mass\ change\ \%\ (m\%) = \frac{m_f - m_s}{m_s}\ x\ 100 \quad (4)$$

Primary aging was concluded after 6 h of NO_2 exposure. Samples after 6 h exposure showed no measurable iodine capture during subsequent iodine capture testing Secondary aging was performed for 6 h for all samples and followed the same procedure as primary aging. Sorbent mass change percentages were found using Eq. 4.

3. Results

3.1. Synthesis of crack-free xerogel membranes

The synthesis of mechanically stable, crack-free xerogel monoliths approx. 10 mm in diameter was demonstrated. A homogenous distribution of Bi-NPs throughout the monolith was achieved by vortexing the sol-gel solution until a spanning gel state was reached. The presence of Bi-NPs in alcogels appeared to assist in the formation of a crack-free monolith by absorbing some of the stress experienced by the silica network during drying process to produce xerogels. The SSAs of these materials ranged between ~200 - 400 $m^2 g^{-1}$, however, no statistical differences were observed between the different samples. The adsorption and desorption isotherms for xerogel with and without porogen is given in Fig. S3 (a and b) in the SI.

Mechanical stability was qualitatively assessed to determine suitability for permeability testing. A pinch test was performed by squeezing the xerogels between two gloved fingers. If no fracture occurred, the xerogels were then dropped from a height of two feet and examined for damage. All xerogels passed both the pinch and drop tests except for TEO, which did not pass either. The addition of bismuth nanoparticles to the xerogels increased the mechanical stability of the xerogels up to 5 w/v% loading. It is believed that similar to their influence during drying, the nanoparticles can absorb stress and inhibit crack propagation [48]. Between 10 – 20 w/v% loading, monoliths could be formed but did not pass the pinch test. Above 20 w/v%, monoliths could not be formed as there appears to not be enough precursor to enable the formation of a robust interconnected network. Due to these findings, 5 w/v% was the maximum Bi-NP loading used for permeability and iodine loading studies.

All xerogels appeared opaque with visible macropores (Fig. 1a). Backlit images of the xerogels (Fig. S3 c and d in the SI) were used to qualitatively assess the microstructure, specifically the pore structure resulting from the porogen. Micrometer-scale pores were clearly observed in TEO but were difficult to distinguish in TEO-2 and TEO-5 due to its dark color from the Bi-NPs. The pore structure of all the xerogels appeared similar to the structure reported in our previous study [47], in which both isolated spherical pores and clusters of pores were observed. The TE and TEO appeared amorphous in XRD while xerogels made with Bi-NPs had peaks corresponding to Bi^0 (Fig. 1b). Rietveld analysis (discussed in Section 3.3 and 3.4) showed that a small fraction of Bi_2O_3 was present. SEM/EDS showed Bi-NPs were homogeneously dispersed throughout the samples with denser Bi-NPs for the 5 w/v% loading compared to the 2 w/v% loading (Fig. 1 c and d).

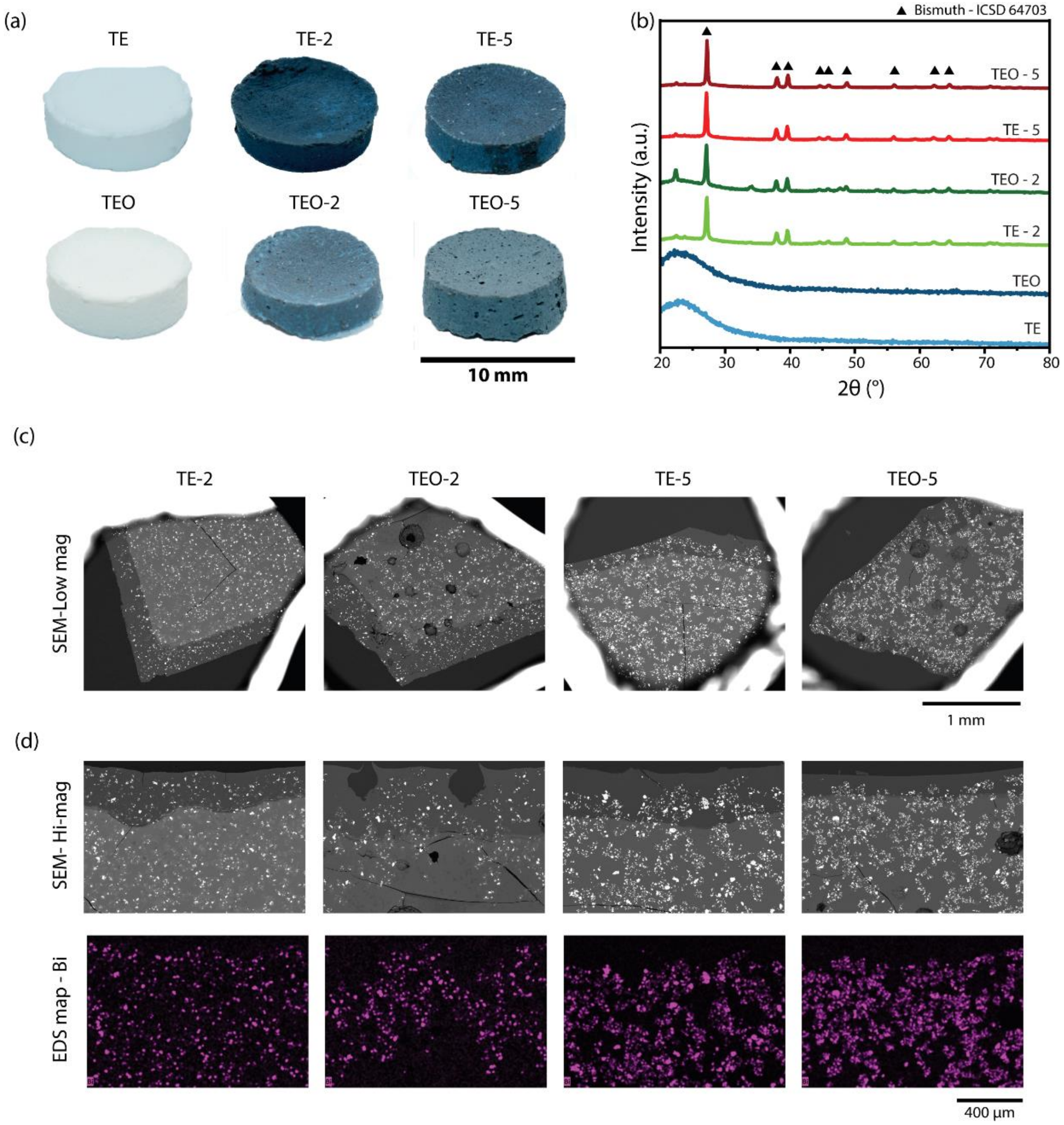

Figure. 1. *(a) Photograph of xerogel monoliths with visible macropores in samples synthesized with oil (TEO, TEO-2 and TEO-5). (b) XRD of xerogels with and without bismuth. Peak patterns in TE-2, TEO-2, TE-5 and TEO-5 correspond with Bi-metal (ICSD 64703) peaks from sample holder is seen in addition to Bi-metal. The amorphous hump in TE and TEO are from the glassy silica xerogel. (c) SEM- Low magnification image (the backscatter detector is visible as the white outline in these images due to the low magnifications). (d) SEM-high magnification images and EDS maps showing dispersion of Bi-NPs in xerogels.*

Based on mass loss observed during DSC/TGA analysis, it is likely that organic residue from either the porogen or heptane might be present in xerogels (Fig. S4 in SI). TEO showed gradual loss of 3 mass% by 150°C, which can be attributed to desorption of physisorbed water. An exothermic peak at 280°C near the regions of the flash points of the porogen was identified followed by gradual, yet steeper, weight loss of an additional 10 mass% by 700°C [50-52]. A less intense and broader exothermic peak is seen at 450°C, which is attributed to decomposition of the silica xerogel [49]. The presence of organic residues in TE and TEO xerogels was confirmed using FTIR, seen predominately at 960 cm^{-1} and 1168 cm^{-1}, both attributed to C–H rocking. (Fig. S5 in SI).

The permeability results for all xerogels are presented in Fig. 2. All xerogel formulations showed permeability values on the order of 10^{-15} m^2. Statistical analysis using a one-way analysis variance (significance level of α = 0.5) showed that there was a statistically significant difference between the TE and Bi-NP loaded xerogels made with the porogen (TEO-2 and TEO-5). Statistical testing was not conducted for the TE-2 and TE-5 because only two data points were collected. The Bi-NPs, in addition to enhancing the mechanical stability of the xerogels (up to 5 w/v%), also appear to cause a slightly more open pore structure. While the porogen does not appear to have a significant impact on the permeability, it was shown to greatly enhance iodine capture (discussed in Section 3.2).

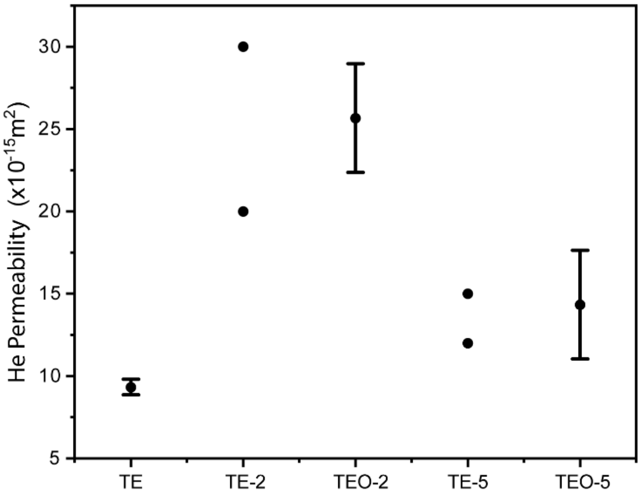

Figure. 2. *He permeability results for all xerogels except for TEO, which did not pass the mechanical testing. Three samples were tested for TE, TEO-2, and TEO-5 with error shown that includes the ±1σ standard deviations. Two samples for TE-2 and TE-5 were tested and both He permeability values are shown.*

3.2. Iodine capture of unaged xerogels and bismuth nanoparticle sorbents

All xerogels changed color after iodine capture performance testing (Fig. 3a). A color change was observed for the TE and TEO xerogels even though no measurable iodine capture was observed. No observable color change occurred after TE and TEO were subjected to a desorption heat treatment (72 h) at 150˚C (Fig. S6 in SI). A return to the original white color was observed after heat treating above 300°C for 6 h. These results indicate that the color change was due to pyrolyzed hydrocarbons from remnants of the porogen and/or solvent and was corroborated by TGA/DSC in Fig. S4 in SI. No crystallinity was detected in the TE and TEO with XRD (Fig. 3b). The color change from blue-green to brown after iodine exposure observed in xerogels containing bismuth nanoparticles is a result of the formation of BiI_3, which was determined using XRD (Fig. 3b).

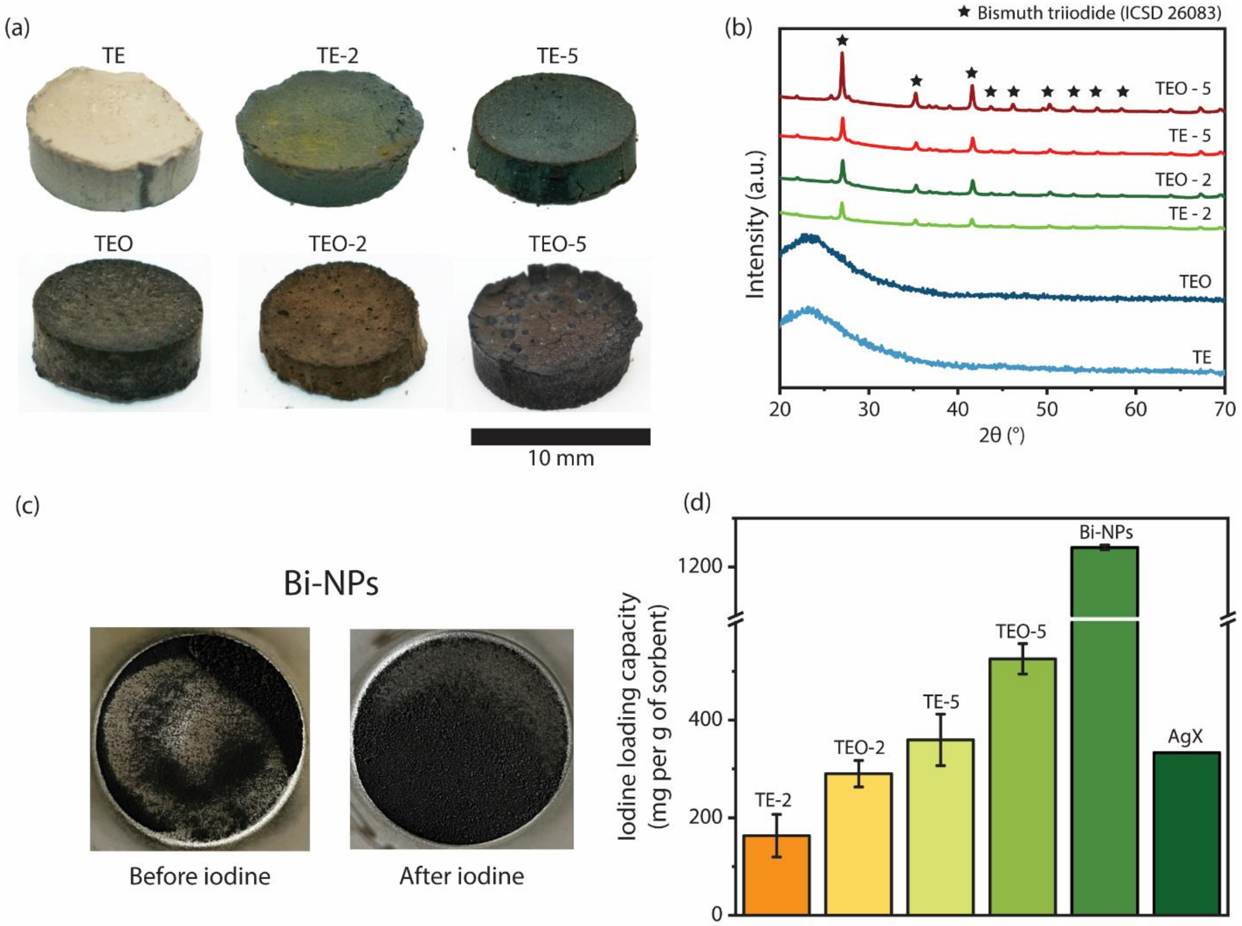

Figure 3. (a) Optical images of xerogels after I_2 exposure. (b) XRD patterns of xerogels after I_2 exposure. Patterns in TE-2, TEO-2, TE-5, and TEO-5 correspond to BiI_3 (ICSD 26083) and the amorphous hump in TE and TEO are from the glassy silica xerogel. (c) Optical images of Bi-NPs before and after iodine capture. (d) Iodine capture capacity of samples represented by the iodine mass captured per unit mass of sorbent (mg I_2 per g of sorbent with standard deviations in parenthesis), TE-2 : 163 (44), TEO-2 : 290 (27), TE-5 : 359 (53), TEO-5 : 526 (31), Bi-NPs: 1298 (24) and AgX : 318 (16). TE and TEO are not shown on the graph because no measurable mass changes were observed after exposure to iodine. XRD pattern of Bi-NPs shown in Fig. S7 (SI).

The iodine loading of Bi-NPs were studied separately from bismuth-loaded xerogels to understand the effects of the sorbent substrate on capture and aging performance. The mass of Bi-NPs (0.05g) used per sample was the same as the mass of bismuth nanoparticles used in synthesizing TEO-5 xerogels to get comparable results. In TEO-5, bismuth nanoparticles constitute 50% of the overall mass of the sorbent. Iodine capture capacity of TEO-5 was recalculated per gram of bismuth (0.05 g) encapsulated per xerogel, at 1156 (±60) mg per g of Bi (see Section 3.4). This result shows that the iodine loading capacity of TEO-5 is 90% (±5%) of the Bi-NPs, which indicates the substrate does little to limit iodine access to bismuth. No color change was observed for Bi-NPs after iodine capture performance testing (Fig. 3c) but this is attributed to the fact that both Bi metal and BiI_3 are black-grey in color. Analysis of the XRD patterns showed that iodine was captured as both BiI_3 and BiOI (see Section 3.4).

For the xerogels, the iodine capture capacity increased with increasing bismuth concentration from 163 (±44) mg g^{-1} for TE-2 to 359 (±53) mg g^{-1} for TE-5 (Fig. 3d). Although no statistically significant differences were observed between the SSAs of the xerogels, the capture performance of xerogels formed with porogens was statistically higher than those of the parent xerogels for each of the respective loadings. TEO-2 (290 [±30] mg g^{-1}) showed an 78% (±18%) increase over TE-2 and TEO-5 (525 [±30] mg g^{-1}) was 47% (±12%) higher than TE-5. The chemisorption of TEO-5 was greater than that of AgX (318 [±16]) and reported by other studies (333.3 [±4.0]) [50]. TEO-5 was selected for additional studies related to aging and phase stability because it showed the greatest amount of iodine chemisorption.

SEM micrographs of TEO-5 (Fig. 4) provided insight into the enhanced iodine capture for samples made with the porogen. In the SEM micrographs (Fig. 4a), both small and large bismuth clusters were observed. Upon examination of an area of larger clusters that exhibited cracking (Fig 4b), it was found that some of the bismuth nanoparticles appeared to line the spherical pores formed by the porogen. This result shows that more bismuth is present to react with iodine in xerogels made with the porogen. It has been reported that physisorption of iodine can be increased by increasing pore volume [26, 51-53]. Iodine physically held within the pores increased the interaction time with the bismuth nanoparticles lining the pore walls, which enabled enhanced iodine capture through chemisorption compared to xerogels made without the porogen.

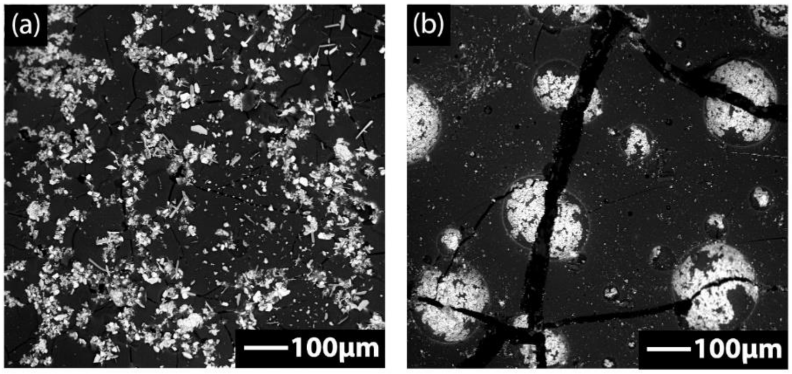

Figure 4. TEO-5 showing Bi-NPs deposited in two different regions of the xerogel. It can be seen that (a) regions without macroscale pores have non clustered distribution while (b) regions with macroscale pores have more concentrated Bi-NPs within the pores.

3.3. Primary aging of Bi-NPs and TEO-5

Aging Bi-NPs and TEO-5 in 1 v/v% NO_2 resulted in an increase in sorbent mass with increasing exposure times (Fig. 5). In Table 3, samples are labeled for the number of hours aged in 1 v/v% NO_2, given as 0 h, 1 h, 3 h, 6 h Bi-NPs and 1 h, 3 h, 6 h TEO-5.

Table 3. sorbent sample list for aging experiments

Sample ID	Substrate	Bi-NPs mass in sample	Hours aged in 1 v/v% NO_2
0 h TEO-5	silica xerogel with porogen	0.05 g	0
1 h TEO-5	silica xerogel with porogen	0.05 g	1
3 h TEO-5	silica xerogel with porogen	0.05 g	3
6 h TEO-5	silica xerogel with porogen	0.05 g	6
0 h Bi-NPs	free bismuth nanoparticles	0.05 g	0
1 h Bi-NPs	free bismuth nanoparticles	0.05 g	1
3 h Bi-NPs	free bismuth nanoparticles	0.05 g	3
6 h Bi-NPs	free bismuth nanoparticles	0.05 g	6

Over a 6 h period, Bi-NPs gained 8 mg ± 0.1 (15.5% [±1.0%]) compared to TEO-5, which gained 5 mg ± 1 (5.3% [±1.0%]). A TEO sample was aged for 6 h to understand the behavior of the substrate and showed a mass loss of 4 mg ± 1 (7.0% [±1%]). Considering the mass loss of the xerogel substrate, the difference between the TEO-5 and Bi-NPs after 6 h is 3.1% (±2.0%).

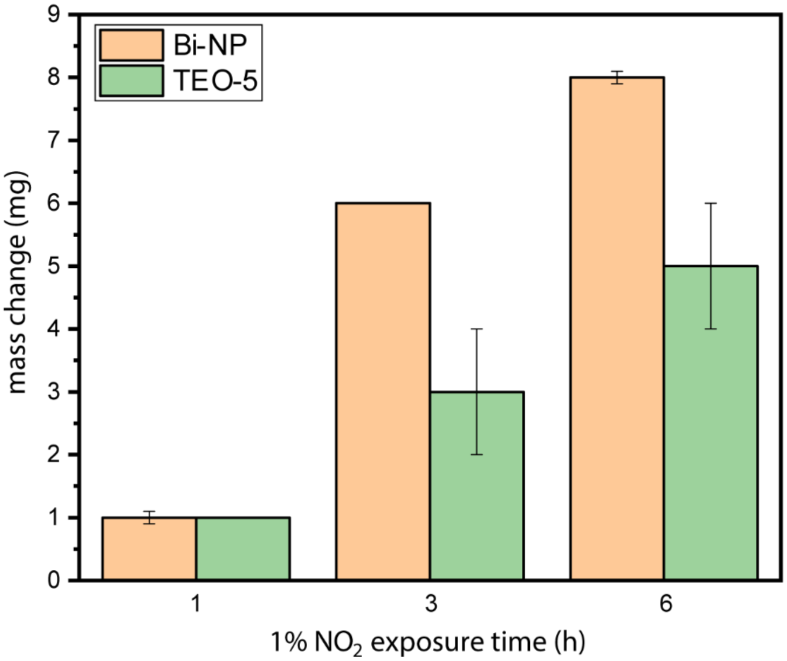

Figure 5. Mass change of samples after aging in 1v/v% NO_2. The mass lost by TEO xerogels was added to the mass change of the TEO-5 xerogel to highlight the change due to bismuth oxidation.

To understand the effects of organic residue on aging, FTIR spectra were collected for Bi-NPs and TEO-5 before and after 1 h of aging in NO_2 (Fig. 6 a and b). Spectra for Bi-NPs showed peaks at 1210 cm^{-1}, which correspond to Bi-OH bond [54]. After aging, a wide peak from the region 1200 cm^{-1} to 1750 cm^{-1} is seen along with a sharp peak at 1210 cm^{-1} indicative of presence of nitrate species. Between 2500 cm^{-1} and 3500 cm^{-1}, –OH peaks appear in aged Bi-NPs [54]. This indicates that the unaged sample contained a small amount of OH species, likely due to the passive oxide layer [54], and increased the amount of oxide in the nanoparticles after aging. Since the ATR limit of detection is < 900 cm^{-1}, the characteristic bond of Bi–O–Bi is not seen in Bi-NPs.

The FTIR of TEO-5 before aging has an -OH peak between 3200 cm^{-1} and 3600 cm^{-1}, which could be from moisture adsorbed in silica or surface OH groups. Peaks from organic residue from oil and heptane can be seen as a peak at 1400 cm^{-1} and 1450 cm^{-1} [55]. Peaks near 1400 cm^{-1} and 1450 cm^{-1} were associated with rocking of C–H bonds of olefins and bending of –CH_2 in aliphatic groups in vegetable oil [56, 57]. Aged TEO-5 have new strong peaks between 1700 cm^{-1} to 1200 cm^{-1} along with peaks associated with Bi–O–Bi bonds in the range 700 cm^{-1} to 400 cm^{-1} [54, 58]. The higher relative intensity of the NO_3^- peak at 1210 cm^{-1} in aged Bi-NPs compared to the wider peaks from 1200 cm^{-1} to 1700 cm^{-1} in aged TEO-5 could indicate increased interaction of NO_2 with xerogel components in TEO-5. The increased contact time of NO_2 in pores of TEO-5 and bismuth lining the pores could promote the formation of bismuth subnitrates compared to formation of primarily Bi_2O_3 in free Bi-NPs [25]. The organic residue from oil could interfere with oxidation of Bi nanoparticles. The combination of these mechanisms could show why TEO-5 captures iodine at higher mg per g of Bi for comparable aging times. XRD was performed to analyze the phases present after primary aging (Fig. 6c and 6d) and Rietveld refinement was used to investigate the extent of oxidation through calculating mass fractions of identified phases (Fig. 6e and 6f). From XRD analysis, 7-8 mass% of Bi_2O_3 was present in unaged Bi-NPs and TEO-5 due to native oxide layers on as-received Bi-NPs. After aging for 1 h, Bi-NPs showed 25% more Bi_2O_3 than TEO-5 and after aging for 3 h, Bi-NPs showed 55% more Bi_2O_3. After 6 h, Bi-NPs showed Bi_2O_3 but the XRD pattern for TEO-5 could not be refined, and this is attributed14 to the formation of amorphous bismuth oxynitrate or bismuth oxide phases. At this point, the samples did not chemisorb iodine and aging was considered complete. XPS was performed to determine the structure of the as- received bismuth nanoparticles. Depth profiling revealed a core-shell structure consisting of a bismuth oxide shell with a bismuth metal core as seen from the evolution of the lower binding energy Bi metal peaks with depth profiling in Fig. 6g. XPS scans of nitrogen 1s peaks in Fig. 6h shows 0 h, 1 h, and 3 h Bi-NPs have no incorporation of nitrogen or nitrates on free Bi-NPs.

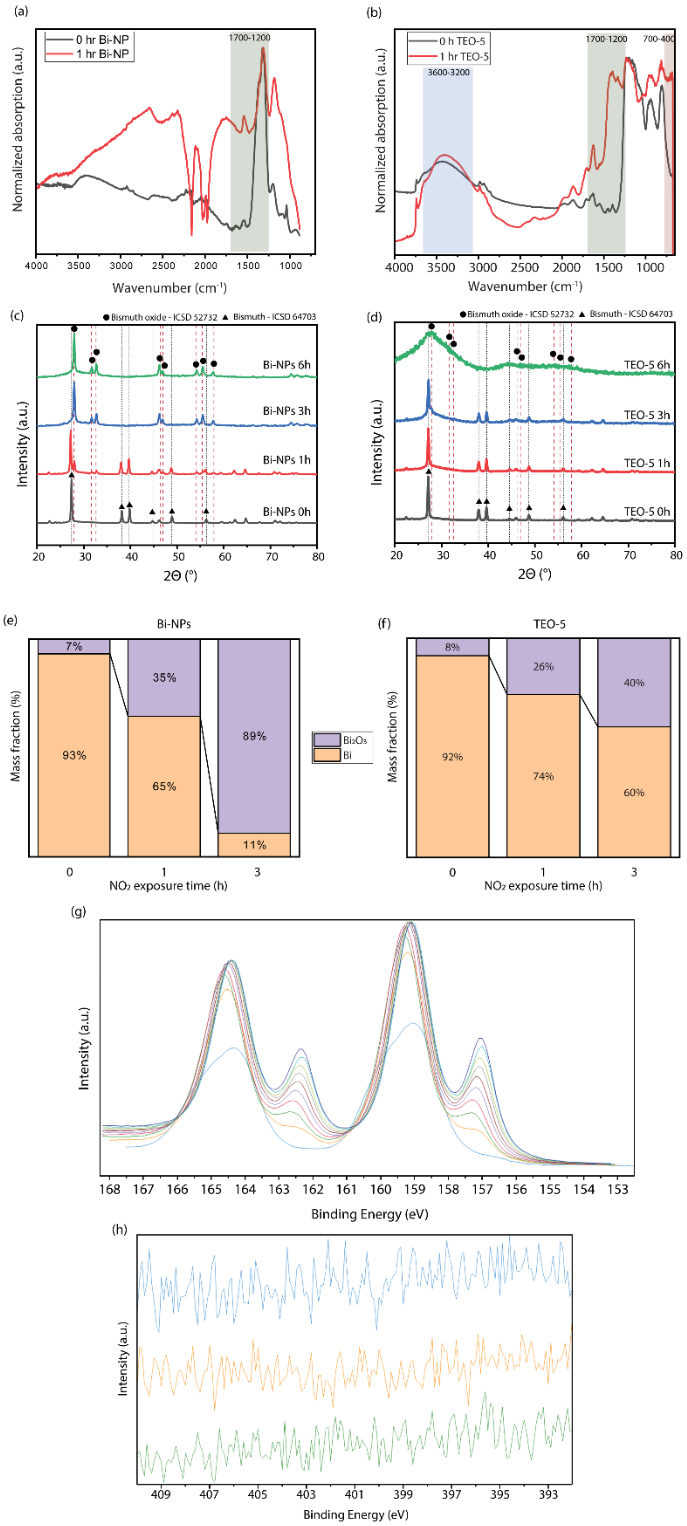

Figure 6. (a) FTIR of Bi-NPs with 0h and 1h of aging in 1 v/v% NO_2 aging. (b) FTIR of TEO-5 with 0h and 1 h aging in 1v/v% NO_2 aging. (c) XRD patterns of Bi-NPs and (d) xerogels after aging in 1v/v% NO_2 showing Bi and Bi_2O_3, ICSD 64703 and ICSD 52732. Rietveld refinement data of (e) Bi-NPs and (f) TEO-5 after 0 h, 1 h, and 3h of 1 v/v% NO_2 aging and (g) Bi 4f XPS spectra of unaged Bi-NPs shows increasing Bi metal peaks with depth profiling and (h) N 1s spectra 0 h, 1 h and 3 h Bi-NPs samples show that there is no incorporation of N (or presence of $BiNO_3$) in the samples after aging.

3.4. Iodine loading of aged Bi-NPs and TEO-5

Figure 7a shows a reduction in iodine capture capacity represented in Q_e (mg g^{-1}) for both Bi-NPs and TEO-5 after NO_2 aging. Due to the incorporation of the xerogel mass in this calculation, TEO-5 shows lower iodine capture for unaged samples. When the iodine capture capacity of unaged TEO-5 is represented in mg of iodine captured per g of bismuth per xerogel (Fig. 7b), TEO-5 shows a reduction of only 10% ±5% compared to unaged Bi-NPs. These results indicate high utilization of the dispersed Bi-NPs in TEO-5. Fig. 7a and 7b also reveal a shallower slope for iodine capture reduction for TEO-5 compared to Bi-NPs through the aging process. Extrapolating trendlines from 0 h to 3 h in Fig. 7b indicated Bi-NPs will no longer capture iodine at ~3.25 h of aging and TEO-5 will no longer capture iodine at ~4.25 h, a 40% increase in bismuth utilization lifetime. By 6h, TEO-5 and Bi-NPs no longer captured iodine and was not used for the trendline.

Figure 7c and 7d show XRD patterns of TEO-5 and Bi-NPs after aging and subsequent iodine loading. Rietveld refinements were performed to quantify identified phases (Fig. 7e and 7f). The relative phases in Bi-NPs are closer to a direct comparison to gravimetric analysis as there were no other materials present that could react during the aging process. Eq. 8 shows that BiOI will form if a 50:50 molar ratio of Bi:Bi_2O_3 ratio is present. Unaged Bi-NPs showed 71 mass% BiI_3 with 29 mass% BiOI due to the passive oxide layer present on the bismuth nanoparticles. The BiOI:BiI_3 mass ratio increased after 1 h due to the higher concentration of Bi_2O_3 initially present. Bi-NPs aged for 3 h showed unreacted Bi_2O_3 along with BiOI, and BiI_3 was not detected. The absence of BiI_3 and presence of 82 mass% Bi_2O_3 shows that significantly less than 50 mol% Bi was present in 3 h Bi-NPs sample. Only 18 mass% BiOI in Bi-NPs 3 h was present, which correlates closely to the gravimetric extrapolation of no iodine capture at ~3.25 h. The phases for the 6 h Bi-NPs could not be quantified due to low peak intensity and the amorphous shoulder present, but XRD patterns indicate oxidation to Bi_2O_3.

In Fig. 7f, unaged TEO-5 showed 92 mass% BiI_3 with 8 mass% BiOI after exposure to iodine. Compared to the Bi-NPs, TEO-5 maintained higher percentages of bismuth capable of participating in iodine capture throughout aging. TEO-5 aged for 1 h showed similar phase percentages as unaged Bi-NPs. TEO-5 aged for 3 h showed complete utilization of bismuth by forming BiI_3 and BiOI. For TEO-5 aged for 6 h, the iodine loading was near zero, and the XRD patterns revealed an amorphous structure that further indicated a change from a crystalline to an amorphous bismuth oxide phase. After aging and iodine loading, TEO-5 xerogels passed the drop and pinch tests described in Section 3.1.

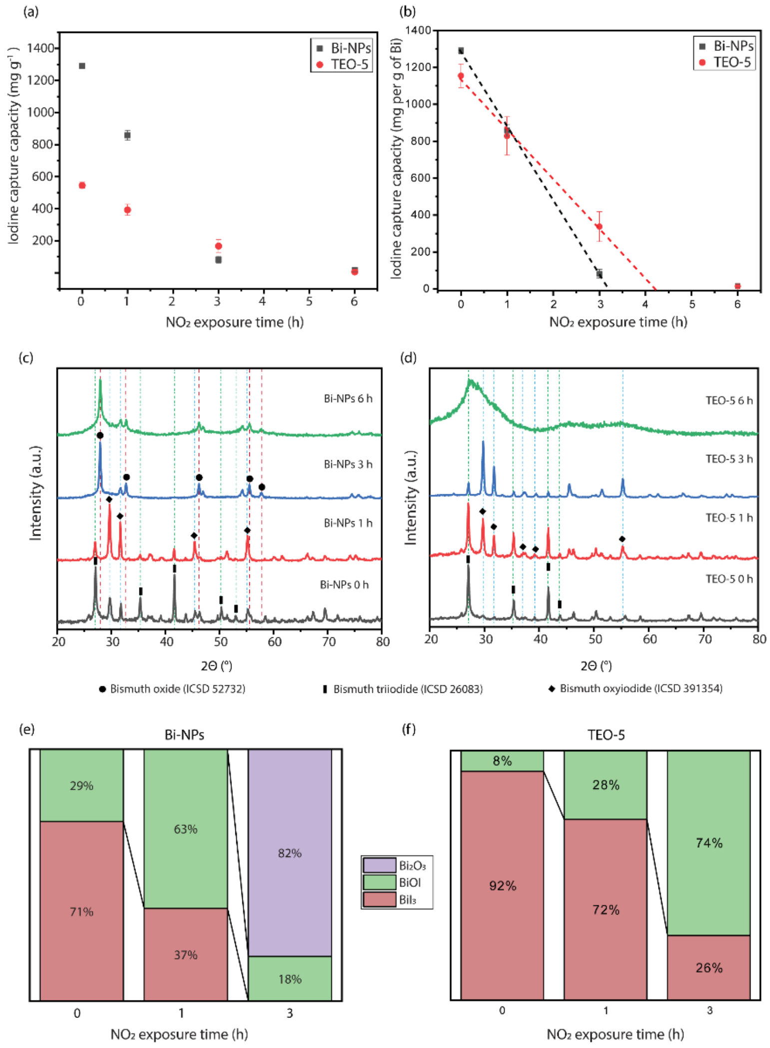

Figure. 7. (a) Iodine capture capacity in mg per g of sorbents aged in 1% NO_2 for 0 h, 1 h, 3 h, and 6 h. (b) Calculated iodine capture capacity in mg per g of bismuth for samples aged in 1% NO_2 for 0h, 1 h, 3 h, 6 h. (c) XRD patterns of Bi-NPs aged in 1% NO_2 for 0 h, 1 h, 3 h, and 6 h. (d) XRD patterns of TEO-5 aged in 1% NO_2 for 0 h, 1 h, 3 h, and 6 h showing BiI_3, BiOI and Bi_2O_3 (ICSD 26083, ICSD 391354 and ICSD 52732). (e) Rietveld refinement of Bi-NPs aged in 1% NO_2 for 0 h, 1 h, and 3 h after iodine exposure. (f) Rietveld refinement of TEO-5 aged in 1% NO_2 for 0 h, 1 h, and 3 h after iodine exposure.

Figure 8a shows the I 3d spectra from 1 h Bi-NPs after iodine exposure. The initial surface spectra from the sample showed the presence of two peaks at 623.6 eV and 631.1 eV. These high values of I 3d binding energies are associated with iodates. In this case, we hypothesize that the outer layers of the sample, as analyzed by XPS, formed a bismuth iodate, which is in agreement with the observed XPS spectrum [59]. To ensure that the bismuth iodate was only formed on the outer layers, the sample was depth profiled. Figure 8b shows the emergence of two new peaks around 619.5 eV and 631 eV. These peaks are associated with iodide in BiOI and BiI_3 [60, 61]. Further depth profiling showed that the original higher binding energy iodate peaks completely disappeared, and the iodine spectra only comprised of the lower binding energy iodide peaks, as seen in Fig. 8c. This result confirms that the outer surface formed a highly oxidized bismuth iodate whereas the bulk Bi-NPs formed a bismuth iodide/oxyiodide.

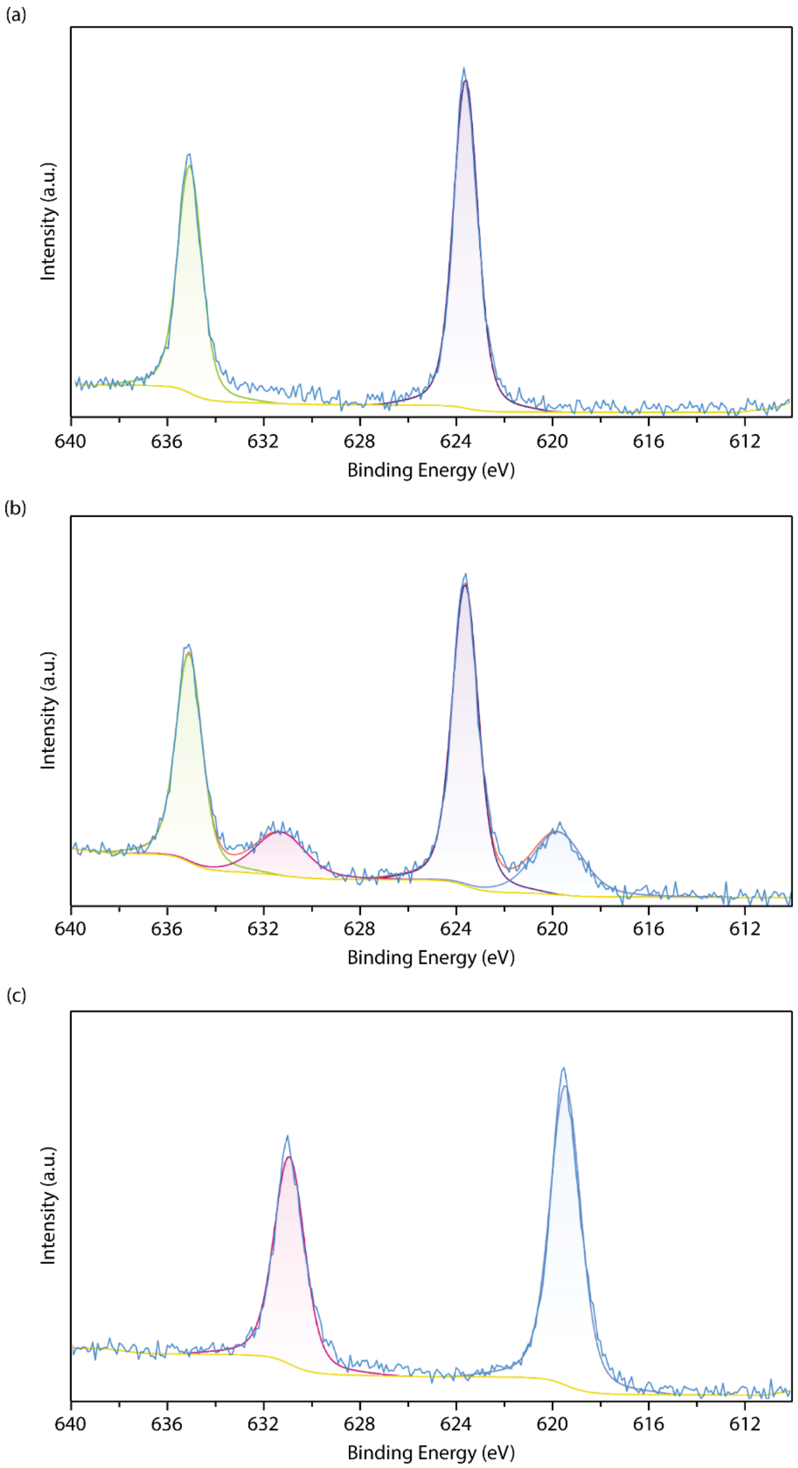

Figure. 8. I 3d spectra of the 1h Bi-NPs after iodine exposure. (a) Sample prior to depth profiling, (b) After 20 seconds of depth profiling, and (c) After 100 seconds of depth profiling.

3.5. Secondary aging

Unaged and aged samples were exposed to 1 v/v% NO_2 to explore the stability of BiI_3, BiOI, and Bi_2O_3 phases. Fig. 9a and 9b show the XRD patterns of samples after secondary aging and the corresponding Rietveld analysis is shown in Fig. 9c and 9d. Rietveld analysis showed the transformation of BiI_3 to BiOI in all samples containing BiI_3 prior to secondary aging (Bi-NPs 0 h, 1 h and TEO-5 0 h, 1 h, 3 h). Rietveld refinement showed that BiOI present in the samples prior to secondary aging remained as BiOI, which indicates the stability of this phase in an oxidizing environment. Bi_2O_3 present in Bi-NPs 3 h prior to secondary aging remained at similar mass loading (±6%), however XRD showed a shift from crystalline to amorphous phases for Bi-NPs 3 h and 6 h and TEO-5 6 h. This shift is congruent with either the formation of bismuth oxynitrates, or the formation of amorphous Bi_2O_3.

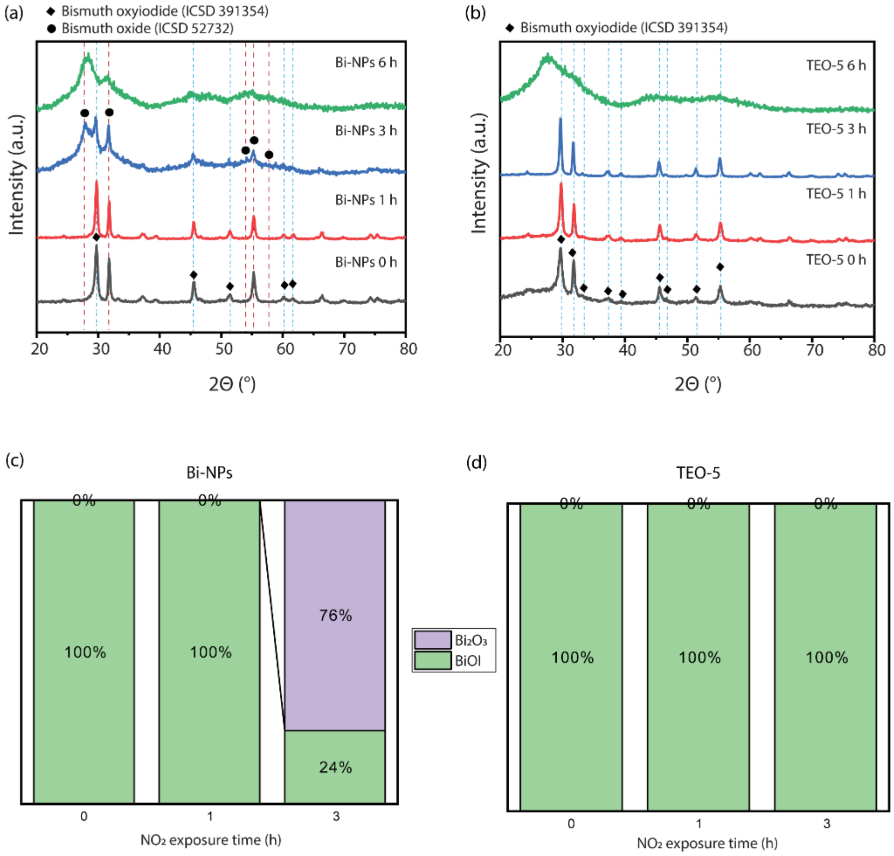

Figure 9. (a) XRD patterns of Bi-NPs after secondary aging showing BiOI in 0 h and 1 h, and Bi_2O_3 in 3 h and 6 h (ICSD 391354 and ICSD 52732). (b) XRD patterns of TEO-5 showing BiOI in 0 h, 1 h, and 3 h, and Bi_2O_3 in 6 h. (c) Rietveld refinement of Bi-NPs after secondary aging in 1 v/v% NO_2. (d) Rietveld refinement of TEO-5 after secondary aging in 1 v/v% NO_2

4. Discussion

4.1. Xerogel microstructure

Obtaining a crack-free silica xerogel monolith via ambient pressure drying can be challenging as the capillary forces experienced by the silica network during drying can lead to pore collapse. We have previously reported a method to synthesize crack-free xerogel monoliths with tunable pore structures without any surface modification by adjusting the vapor pressure during drying [47]. Despite the presence of a thin oxide layer on the bismuth nanoparticles, the direct incorporation of bismuth nanoparticles removes the uncertainty associated with incorporating Bi^0 through bismuth nitrate reduction techniques [26]. Bismuth nanoparticles and clusters were strongly embedded within the silica matrix, remaining in place after sample preparation using mechanical polishing.

While there were no statistically significant differences in the SSAs between samples, the effects of adding Bi-NPs were observed through statistically significant differences in measured permeabilities. The presence of Bi-NPs in the pores of xerogel creates microcracks, which creates more paths for gas flow, resulting in increased permeability. In addition to increased permeability, Bi-NPs also likely reinforced the silica network and helped prevent pore collapse during ambient pressure drying. This reinforcement provided by Bi-NPs created mechanically stable xerogel up to 5 w/v% of Bi-NPs. Further addition of Bi-NPs created mechanically weak gels, as there is not enough silica network to support the weight of Bi-NPs.

When soybean oil is added as a porogen during silica gel synthesis, it creates macro-scale pores, lowering the mechanical strength in TEO xerogels as oil pores closer to other pores can cause catastrophic pore collapse of silica pore walls in xerogels. Bi-NPs likely stabilized the oil during the sol-gel reaction through the Pickering effect in TEO-2 and TEO-5, leading to the stable and separated pores in the xerogels [62]. These isolated pores avoid a catastrophic collapse of pore walls and improved mechanical strength enough to complete the permeability testing of TEO-2 and TEO-5. The Bi-NPs stabilizing the oil during the sol-gel reaction were lining the pores in the SEM of xerogel. The presence of pores lined with Bi-NPs can have improved access for iodine species through deeper diffusion and enhanced iodine capture in TEO-2 and TEO-5 compared to TE-2 and TE-5.

The heptane used in the sample preparation process acted as a low surface tension solvent and helped in achieving a xerogel monolith. The organic residues left by heptane inhibited accurate characterization of skeletal density. It also appears that the organic residues aided in extending the life of Bi-NPs during aging. While the porogen did not create interconnected macropores, the cluster of Bi-NPs surrounding the macroscale pores along with microcracks inside the monolith improved iodine capture.

4.2. Aging and iodine capture

HSC software was coupled with experimental characterization to understand the chemical reactions occurring during aging, iodine exposure, and secondary aging (Table 1 in Section 1 and Table S1-S6 in SI). Both Bi-NPs and TEO-5 formed Bi_2O_3 during primary aging. The increase in Bi_2O_3 formation yielded lower percentages of BiI_3 and increasing percentages of BiOI and Bi_2O_3 or bismuth oxynitrate after iodine loading. After secondary aging, BiI_3 transformed to BiOI, with BiOI present prior to secondary aging remaining unchanged. Bismuth oxide or oxynitrate present prior to secondary aging remained but further aging in 1 v/v% NO_2 changed the phase from crystalline to amorphous. The digital photograph in Fig. 10 shows that oxidized Bi-NPs change color from black to yellow, characteristic of Bi_2O_3, while oxidized TEO-5 shows a partial change in color from black to white, characteristic of bismuth oxynitrates or bismuth oxides formed from heat treating bismuth oxynitrates at 150°C. Analysis of XRD patterns and optical imaging in Fig. S8 in SI show the formation of yellow, crystalline Bi_2O_3 after aging TEO-5 in air at 150°C for one week. The 3 h aged TEO-5 shows color change from black and white to uniform brown color. This uniform product shows that when immobilized within the xerogel matrix, Bi and Bi_2O_3 or bismuth nitrate reacted in the presence of iodine to form BiOI.

Figure 10. Optical images of (top) Bi-NPs and (bottom) TEO-5 after primary aging, iodine exposure, and secondary aging. Xerogels that appeared heterogenous in color did not show any effect on iodine loading capacity compared to xerogels that appeared homogenous.

For primary aging, equilibrium compositions calculated using HSC (Table S3 in SI. and Eq. 5 and 6) indicate that exposing bismuth metal to NO_2 will yield Bi_2O_3 and N_2 gas. Experimental NO_2 exposure yielded bismuth oxide in Bi-NPs and amorphous bismuth oxide in TEO-5. However, HSC does not include bismuth nitrates, so we were unable to explore equilibriums of bismuth nitrate products identified in TEO-5 xerogels. It was found that the oxidation rate was lower for TEO-5 compared to Bi-NPs.

The reaction calculated using HSC (Eq.7) for the formation of BiI_3 from unaged bismuth samples after iodine exposure were verified experimentally. However, up to 29 mass% BiOI was formed due a passive oxide layer present on as-received bismuth nanoparticles. Consistent decrease in iodine sorption values is seen with aging of both Bi-NPs and TEO-5, although TEO-5 shows slower decline in iodine capture capacity over time. By comparing Bi-NPs and xerogels, it was identified that dispersing bismuth nanoparticles throughout the xerogel decreased unaged iodine loading capacity by 10% but maintained higher iodine loading capacity after aging.

For iodine exposure, equilibrium compositions calculated using HSC (Table S.4 and S.5) agreed with results in the literature in that exposing bismuth to iodine will result in (a) BiI_3 if only bismuth is present, (b) BiOI if 50 mol% Bi_2O_3 and 50 mol% Bi (69 mass% Bi_2O_3 and 31 mass % Bi) are present (Eq. 8 and 9), or (c) no reaction if only Bi_2O_3 is present (Eq. 12) [26]. Samples with Bi:Bi_2O_3 molar ratios between these three points were found to show a relative amount of either BiI_3 and BiOI, or BiOI and Bi_2O_3. Experimental results showed maximum BiOI formation in 3 h TEO-5, which contained 40 mol% Bi (60 wt.%) prior to iodine exposure. However, as BiI_3 was also seen in this sample after iodine exposure, TEO-5 could have been further oxidized for some time between 3-6 h to form more BiOI. Equations 8 and 9 calculated using HSC show BiOI formation could occur via a combined reaction of Bi, Bi_2O_3, and I_2, or via BiI_3 reacting with Bi_2O_3. The BiI_3 and Bi_2O_3 were not identified together in any samples at any time, indicating the reactivity of BiI_3 and Bi_2O_3 to form BiOI. While it is unknown if BiI_3 must be formed as an intermediate, or if Bi_2O_3 can react with Bi and I_2 simultaneously, the final product was established as thermodynamically stable BiOI. For Bi-NPs immobilized in the xerogel substrate, BiOI is likely formed from a core-shell structure of Bi-Bi_2O_3 identified through XRD and XPS. Based on the XPS and XRD results, we hypothesize that the oxygen is successively replaced by iodine; iodine to oxygen atomic ratio starts with 0:1 when it is bismuth oxide and proceeds to 1:3 for iodate, then to 1:1 for oxyiodide, and finally to 3:0 for bismuth iodide. Verification of this mechanism will require studying the reaction using in situ techniques in future. TEO-5 allowed for complete utilization of metal sorbent after aging at times when Bi-NPs did not. This can be seen best after 3 h aging, where Bi-NPs formed Bi_2O_3 but TEO-5 formed BiI_3 and BiOI. The above findings reveal valuable information as to the lifetime of bismuth metal in relation to its ability to capture iodine.

For secondary aging, equilibrium compositions calculated using HSC (Table S6 in SI) indicate that exposing BiI_3 to NO_2 will yield BiOI, Bi_2O_3, and Bi_5O_7I as physical phases and release molecular $I_{2(g)}$. The formation of Bi_5O_7I and Bi_2O_3 during secondary aging was not seen in this study but rather the formation of stable BiOI (Eq. 13,14). BiOI was not found to oxidize further to Bi_2O_3 or Bi_5O_7I.

Although unaged samples showed higher iodine loading than aged samples through formation of BiI_3, all BiI_3 samples were transformed to BiOI, indicating that iodine was lost (likely as $I_{2(g)}$) during secondary aging. HSC (Eq. 13,14) mass balance calculations show BiI_3 loses 40.3 mass when reacting with NO_2 to form BiOI through a 43.0 mass decrease in I_2 and 2.7 mass increase in O_2. While gravimetric analysis could show error after secondary aging due to the addition of oxygen (Table 4), preliminary results of unaged Bi-NPs and TEO-5 showed up to 39 mass% and 30 mass% losses, respectively. The trends for converting BiI_3 in a sample to BiOI was also verified through XRD and Rietveld refinement. Samples that showed high percentages of BiOI prior to secondary aging did not show any change other than forming more BiOI with available BiI_3, and corresponding percent mass loss. These results highlight BiI_3 is a thermodynamically unstable phase under elevated temperatures and exposure to NO_2. According to HSC mass balance, iodine capture capacity after secondary aging will be equivalent regardless of initial iodine capture phase, be it BiI_3 or BiOI. While Rietveld refinement indicates these reactions (Eq. 7, 8, 9), gravimetric results are not conclusive enough for total verification. However, these results indicate that full utilization of the sorbent, given by the restrictions of the environment, can be made even after significant aging has occurred. Under the testing conditions, the highest theoretical mg per g of Bi iodine loading achievable by bismuth is 564 mg per g of Bi due to the one-to-one bismuth-iodine coordination of BiOI rather than 1822 mg per g of Bi theoretically achievable by one-to-three bismuth-iodine molar ratio of BiI_3.

Table 4. Secondary aging gravimetric analysis where $m_{L,sa}$ is the mass loss after secondary aging (mass%).

Sample Name	***$m_{L,sa}$ (mass%)***
0 h TEO-5	*-30, -31*
1 hTEO-5	*-22, -19*
3 h TEO-5	-10, -8
6h TEO-5	*-2, -2*
0h Bi-NPs	*-39, -37*
1 h Bi-NPs	*-23, -22*
3 h Bi-NPs	*1, 2*
6 h Bi-NPs	*1, 2*

5. Summary and conclusions

Mechanically robust xerogels were prepared with up to 5 w/v % Bi-NPs and soybean oil as a porogen. The addition of more than 5 w/v % Bi NPs created a weak and delicate xerogel with low mechanical integrity (high friability). The addition of soybean oil reduced the robustness yet yielded a monolith with higher iodine capture. The successful and rapid synthesis of a monolithic silica xerogels with few processing steps could be beneficial for commercial production.

The iodine capture capacity was studied for unaged xerogels and xerogels aged in 1 v/v% NO_2 at 150°C. Most of the iodine was captured in unaged xerogels as BiI_3, and a combination of BiI_3 and BiOI was found in aged xerogels. The unaged Bi-NPs captured iodine as both BiI_3 and BiOI. While the BiOI content increased proportionally with aging time for both Bi-NPs and xerogels, Bi-NPs showed faster aging compared to Bi-NPs loaded in xerogels. It was determined that BiI_3 was not a stable phase and transformed to BiOI during the secondary aging process. This indicates that iodine captured as BiOI is desired over BiI_3 to prevent the loss of captured iodine as $I_2(g)$.

HSC provided a robust framework for the reactions studied in this work. However, some of the HSC predictions were not observed, such as the formation of Bi_5O_7I or the oxidation of BiOI to Bi_2O_3 during secondary aging. While this work showed the importance of capturing iodine as BiOI, studies using in situ characterization should be performed to further understand the underlying mechanisms of these phase transformations.

Acknowledgements

This work was supported by the United States Department of Energy (DOE) Nuclear Energy University Program (NEUP) under contracts DE-NE0008900 and DE-NE0008236, the WTP project office in the DOE Office of River Protection managed by Albert Kruger under contract 89304021CEM000014, and the US Nuclear Regulatory Commission (USNRC) under contract 31310022M015. Dr. Kenny Osborne and Ms. Nancy Hebron-Isreal serve as the program managers for the DOE and NRC awards, respectively. Pacific Northwest National Laboratory (PNNL) is operated by Battelle Memorial Institute for the DOE under contract DE-AC05–76RL01830. The purchase of the X-ray photoelectron spectrometer, housed in the Materials and Electrochemical Research Laboratory, was supported by the National Science Foundation through NSF MRI award 2117820.

References

1. Brook, B.W., et al., *Why nuclear energy is sustainable and has to be part of the energy mix.* Sustainable Materials and Technologies, 2014. **1-2**: p. 8-16.
2. Center, B.P., *Annual energy outlook 2020.* Energy Information Administration, Washington, DC, 2020. **12**: p. 1672-1679.
3. Lawson, A., *Decarbonizing US power.* Climate innovation, 2018. **2050**.
4. Bertelsen, E.R., et al., *Electrochemistry of PUREX: R is for reduction and ion transfer.* Solvent Extraction and Ion Exchange, 2022. **40**(1-2): p. 64-85.
5. McKibben, J.M., *Chemistty of the purex process.* Radiochimica Acta, 1984. **36**(1-2): p. 3-16.
6. Henrich, E., et al., *Improved iodine and tritium control in reprocessing plants*. 1981.

7. Riley, B.J., et al., *Evaluation of Getter Metals in Na-Al-Si-O Aerogels and Xerogels for the Capture of Iodine Gas*, in *ACS Applied Materials and Interfaces*. 2020, American Chemical Society. p. 19682-19692.
8. Bruffey, S.H., et al., *A Literature Survey to Identify Potentially Volatile Iodine-Bearing Species Present in Off-Gas Streams*. 2015, Office of Scientific and Technical Information (OSTI).
9. Paviet-Hartmann, P., W. Kerlin, and S. Bakhtiar, *Treatment of gaseous effluents issued from recycling–A review of the current practices and prospective improvements.* 2010.
10. Jubin, R., A. Jordan, and S. Bruffey, *Testing of an iodine and tritium removal system for advanced tritium pretreatment off-gas*. 2018, U.S. Department of Energy, Oak Ridge National Laboratory.
11. Yadollahi, M., H. Hamadi, and V. Nobakht, *Capture of iodine in solution and vapor phases by newly synthesized and characterized encapsulated Cu2O nanoparticles into the TMU-17-NH2 MOF.* Journal of Hazardous Materials, 2020. **399**: p. 122872.
12. Chen, G., et al., *Pitch-based porous polymer beads for highly efficient iodine capture.* Journal of Hazardous Materials, 2022. **434**: p. 128859.
13. Liu, B., et al., *High efficient adsorption and storage of iodine on S, N co-doped graphene aerogel.* Journal of hazardous materials, 2019. **373**: p. 705-715.
14. Zhao, Q., et al., *Controllable Synthesis of Porous Cu-BTC@polymer Composite Beads for Iodine Capture.* ACS Applied Materials & Interfaces, 2019. **11**(45): p. 42635-42645.
15. Jiang, M., et al., *Novel synthesis of NaY-NH4F-Bi2S3 composite for enhancing iodine capture.* Chemical Engineering Journal, 2022. **443**.
16. Jordan, J.A. and R.T. Jubin. *Stability of Tritium and Iodine Sorbents in TPOG Conditions*. 2017. Oak Ridge, TN (United States).
17. Muhire, C., et al., *An overview on metal Oxide-based materials for iodine capture and storage*, in *Chemical Engineering Journal*. 2022, Elsevier B.V. p. 133816.
18. Tesfay Reda, A., et al., *Bismuth-impregnated aluminum/copper oxide-pillared montmorillonite for efficient vapor iodine sorption*, in *Separation and Purification Technology*. 2021, Elsevier B.V. p. 118848.
19. Umadevi, K. and D. Mandal, *Performance of radio-iodine discharge control methods of nuclear reprocessing plants*, in *Journal of Environmental Radioactivity*. 2021, Elsevier Ltd. p. 106623.
20. Wiechert, A.I., et al., *Capture of Iodine from Nuclear-Fuel-Reprocessing Off-Gas: Influence of Aging on a Reduced Silver Mordenite Adsorbent after Exposure to NO/NO2.* Acs Applied Materials & Interfaces, 2020. **12**(44): p. 49680-49693.
21. Choi, S., Y. Nan, and L.L. Tavlarides, *Kinetics of aging process on reduced Ag exchanged mordenite in dry air and humid air.* AIChE Journal, 2021. **67**(8).
22. Choi, S., Y. Nan, and L.L. Tavlarides, *Aging kinetics on silver-functionalized silica aerogel in off-gas streams including dry air, humid air, NO and NO2.* Chemical Engineering Journal Advances, 2021. **8**: p. 100191.
23. Matyáš, J., E.S. Ilton, and L. Kovařík, *Silver-functionalized silica aerogel: towards an understanding of aging on iodine sorption performance.* RSC Advances, 2018. **8**(56): p. 31843-31852.
24. Bruffey, S.H., K.K. Patton, and R.T. Jubin, *Complete Iodine Loading of NO Aged Ag^0-functionalized Aerogel*. 2015, Office of Scientific and Technical Information (OSTI).
25. Asmussen, R.M., et al., *Silver-functionalized silica aerogels and their application in the removal of iodine from aqueous environments.* Journal of hazardous materials, 2019. **379**: p. 119364.
26. Yang, J.H., et al., *Novel synthesis of bismuth-based adsorbents for the removal of 129I in off-gas.* Journal of Nuclear Materials, 2015. **457**: p. 1-8.
27. Zou, H., et al., *Novel synthesis of Bi-Bi2O3-TiO2-C composite for capturing iodine-129 in off-gas.* Journal of hazardous materials, 2019. **365**: p. 81-87.

28. Xian, Q., et al., *Facile synthesis of novel Bi0-SBA-15 adsorbents by an improved impregnation reduction method for highly efficient capture of iodine gas.* Journal of Hazardous Materials, 2022. **424**: p. 127678.
29. Yang, J.H., et al., *Bismuth-embedded SBA-15 mesoporous silica for radioactive iodine capture and stable storage*, in *Journal of Nuclear Materials*. 2015, Elsevier B.V. p. 556-564.
30. Al-Mamoori, A., et al., *Development of bismuth-mordenite adsorbents for iodine capture from off-gas streams.* Chemical Engineering Journal, 2020. **391**: p. 123583.
31. Baskaran, K., et al., *Evaluating the Physisorption and Chemisorption of Iodine on Bismuth-Functionalized Carbon Foams.* ACS Materials Letters, 2022. **4**: p. 1780-1786.
32. Tian, Z., et al., *Comprehensive comparison of bismuth and silver functionalized nickel foam composites in capturing radioactive gaseous iodine*, in *Journal of Hazardous Materials*. 2021, Elsevier B.V. p. 125978.
33. Chee, T.S., et al., *Efficient capture of radioactive iodine by a new bismuth-decorated electrospinning carbon nanofiber*, in *Journal of Nuclear Materials*. 2020, Elsevier B.V.
34. Tian, Z., et al., *Novel bismuth-based electrospinning materials for highly efficient capture of radioiodine*, in *Chemical Engineering Journal*. 2021, Elsevier B.V. p. 128687.
35. Han, S., W. Um, and W.-S. Kim, *Development of bismuth-functionalized graphene oxide to remove radioactive iodine.* Dalton Transactions, 2019. **48**(2): p. 478-485.
36. Matyas, J., et al. *Functionalised silica aerogels: Advanced materials to capture and immobilise radioactive iodine*. in *Ceramic Engineering and Science Proceedings*. 2011. American Ceramic Society, Inc., 735 Ceramic Place Westerville OH 43081 ….
37. Li, M., et al., *A novel nanocomposite based silica gel/graphene oxide for the selective separation and recovery of palladium from a spent industrial catalyst.* Chemical Engineering Journal, 2020. **386**: p. 123947.
38. Mineo, H., et al., *A simple model predicting iodine profile in a packed bed of silica-gel impregnated with silver nitrate.* Journal of nuclear science and technology, 2002. **39**(3): p. 241-247.
39. Wang, D., et al., *Aqueous phase adsorption of toluene in a packed and fluidized bed of hydrophobic aerogels.* Chemical Engineering Journal, 2011. **168**(3): p. 1201-1208.
40. Soelberg, N. and T. Watson, *Deep bed adsorption testing using silver-functionalized aerogel*. 2012, Idaho National Lab.(INL), Idaho Falls, ID (United States).
41. Hosticka, B., et al., *Gas flow through aerogels.* Journal of non-crystalline solids, 1998. **225**: p. 293-297.
42. Beurroies, I., et al., *Gas permeability of partially densified aerogels.* Journal of non-crystalline solids, 1995. **186**: p. 328-333.
43. Baskaran, K., et al., *Sol-gel derived silica: A review of polymer-tailored properties for energy and environmental applications.* Microporous and Mesoporous Materials, 2022: p. 111874.
44. Reynes, J., T. Woignier, and J. Phalippou, *Permeability measurement in composite aerogels: application to nuclear waste storage.* Journal of non-crystalline solids, 2001. **285**(1-3): p. 323-327.
45. Woignier, T., et al., *The use of silica aerogels as host matrices for chemical species: Different ways to control the permeability and the mechanical properties.* Journal of non-crystalline solids, 2004. **350**: p. 299-307.
46. Kim, S.J., G. Chase, and S.C. Jana, *Polymer aerogels for efficient removal of airborne nanoparticles.* Separation and Purification Technology, 2015. **156**: p. 803-808.
47. Baskaran, K., et al., *Membrane synthesis via in-situ pore formation in silica gels through dynamic miscibility with soybean oil.* Colloids and Surfaces A: Physicochemical and Engineering Aspects, 2022. **636**: p. 128183.

48. Etienne, P., et al., *Slow crack growth in aerogels*, in *Journal of Non-Crystalline Solids*. 1995. p. 19-26.
49. Yang, K., et al., *Structural analysis of embedding polyethylene glycol in silica aerogel.* Microporous and Mesoporous Materials, 2021. **310**.
50. Riley, B.J., et al., *Silver-Loaded Xerogel Nanostructures for Iodine Capture: A Comparison of Thiolated versus Unthiolated Sorbents.* ACS Applied Nano Materials, 2022. **5**(7): p. 9478-9494.
51. Liu, N., et al., *Construction of Microporous Lignin-Based Hypercross-Linked Polymers with High Surface Areas for Enhanced Iodine Capture.* ACS Applied Polymer Materials, 2021. **3**(4): p. 2178-2188.
52. Chen, P., et al., *Iodine Capture Using Zr-Based Metal–Organic Frameworks (Zr-MOFs): Adsorption Performance and Mechanism.* ACS Applied Materials & Interfaces, 2020. **12**(18): p. 20429-20439.
53. Wang, L.Y., et al., *Thiophene-based MOFs for iodine capture: Effect of pore structures and interaction mechanism.* Chemical Engineering Journal, 2021. **425**.
54. Astuti, Y., et al. *Synthesis of α-Bismuth oxide using solution combustion method and its photocatalytic properties*. in *IOP Conference Series: Materials Science and Engineering*. 2016. IOP Publishing.
55. Yang, H., J. Irudayaraj, and M.M. Paradkar, *Discriminant analysis of edible oils and fats by FTIR, FT-NIR and FT-Raman spectroscopy.* Food Chemistry, 2005. **93**(1): p. 25-32.
56. Kaur, A., et al., *Changes in chemical properties and oxidative stability of refined vegetable oils during short‐term deep‐frying cycles.* Journal of Food Processing and Preservation, 2020. **44**(6).
57. Guillen, M.D. and N. Cabo, *Some of the most significant changes in the Fourier transform infrared spectra of edible oils under oxidative conditions.* Journal of the Science of Food and Agriculture, 2000. **80**(14): p. 2028-2036.
58. Zulkifli, Z.A., K.A. Razak, and W.N.W.A. Rahman. *The effect of reaction temperature on the particle size of bismuth oxide nanoparticles synthesized via hydrothermal method*. in *AIP Conference Proceedings*. 2018. Author(s).
59. Ji, Z., et al., *Fabrication of Carbon-Modified BiOI/BiOIO3 Heterostructures With Oxygen Vacancies for Enhancing Photocatalytic Activity.* Catalysis Letters, 2018. **148**(11): p. 3349-3362.
60. Boopathi, K.M., et al., *Solution-processable bismuth iodide nanosheets as hole transport layers for organic solar cells.* Solar Energy Materials and Solar Cells, 2014. **121**: p. 35-41.
61. Intaphong, P., et al., *Sonochemical synthesis and characterization of BiOI nanoplates for using as visible-light-driven photocatalyst.* Materials Letters, 2018. **213**: p. 88-91.
62. Salaün, F., C. Butstraen, and E. Devaux, *Sol-Gel Microencapsulation Based on Pickering Emulsion*, in *Science and Technology Behind Nanoemulsions*. 2018, InTech.